

# Polarization-independent dual-band infrared perfect absorber based on a metal-dielectric-metal elliptical nanodisk array

Bingxin Zhang,<sup>1,2</sup> Yanhui Zhao,<sup>2</sup> Qingzhen Hao,<sup>2</sup> Brian Kiraly,<sup>2</sup> Iam-Choon Khoo,<sup>3</sup> Shufen Chen,<sup>1</sup> and Tony Jun Huang<sup>2,\*</sup>

<sup>1</sup>*School of Optoelectronics, Beijing Institute of Technology, Beijing 100081, China*

<sup>2</sup>*Department of Engineering Science and Mechanics, The Pennsylvania State University, University Park, PA 16802, USA*

<sup>3</sup>*Department of Electrical Engineering, The Pennsylvania State University, University Park, PA 16802, USA*  
*\*junhuang@engr.psu.edu*

**Abstract:** We have designed and fabricated a dual-band plasmonic absorber in the near-infrared by employing a three-layer structure comprised of an elliptical nanodisk array on top of thin dielectric and metallic films. Finite difference time domain (FDTD) simulations indicate that absorption efficiencies greater than 99% can be achieved for both resonance frequencies at normal incidence and the tunable range of the resonant frequency was modeled up to 700 nm by varying the dimensions of the three-layer, elliptical nanodisk array. The symmetry in our two-dimensional nanodisk array eliminates any polarization dependence within the structure, and the near-perfect absorption efficiency is only slightly affected by large incidence angles up to 50 degrees. Experimental measurements demonstrate good agreement with our simulation results.

© 2011 Optical Society of America

**OCIS codes:** (50.6624) Subwavelength structures; (250.5403) Plasmonics; (300.1030) Absorption; (160.3918) Metamaterials

---

## References and links

1. K. Nakayama, K. Tanabe, and H. A. Atwater, "Plasmonic nanoparticle enhanced light absorption in GaAs solar cells," *Appl. Phys. Lett.* **93**(12), 121904 (2008).
2. K. R. Catchpole and A. Polman, "Plasmonic solar cells," *Opt. Express* **16**(26), 21793–21800 (2008).
3. J. N. Munday and H. A. Atwater, "Large integrated absorption enhancement in plasmonic solar cells by combining metallic gratings and antireflection coatings," *Nano Lett.* **11**(6), 2195–2201 (2011).
4. T. J. Yen, W. J. Padilla, N. Fang, D. C. Vier, D. R. Smith, J. B. Pendry, D. N. Basov, and X. Zhang, "Terahertz magnetic response from artificial materials," *Science* **303**(5663), 1494–1496 (2004).
5. J. Hao, J. Wang, X. Liu, W. J. Padilla, L. Zhou, and M. Qiu, "High performance optical absorber based on a plasmonic metamaterial," *Appl. Phys. Lett.* **96**(25), 251104 (2010).
6. A. Ishikawa, S. Zhang, D. A. Genov, G. Bartal, and X. Zhang, "Deep subwavelength terahertz waveguides using gap magnetic plasmon," *Phys. Rev. Lett.* **102**(4), 043904 (2009).
7. S. Xiao, U. K. Chettiar, A. V. Kildishev, V. Drachev, I. C. Khoo, and V. M. Shalaev, "Tunable magnetic response of metamaterials," *Appl. Phys. Lett.* **95**(3), 033115 (2009).
8. J. H. Lee, J. Blair, V. A. Tamma, Q. Wu, S. J. Rhee, C. J. Summers, and W. Park, "Direct visualization of optical frequency invisibility cloak based on silicon nanorod array," *Opt. Express* **17**(15), 12922–12928 (2009).
9. Z. Yu, G. Veronis, S. Fan, and M. L. Brongersma, "Design of midinfrared photodetectors enhanced by surface plasmons on grating structures," *Appl. Phys. Lett.* **89**(15), 151116 (2006).
10. J. Rosenberg, R. V. Shenoi, T. E. Vandervelde, S. Krishna, and O. Painter, "A multispectral and polarization-selective surface-plasmon resonant midinfrared detector," *Appl. Phys. Lett.* **95**(16), 161101 (2009).
11. S. Zhu, F. Li, C. Du, and Y. Fu, "A localized surface plasmon resonance nanosensor based on rhombic Ag nanoparticle array," *Sens. Actuators B Chem.* **134**(1), 193–198 (2008).
12. N. Liu, M. Mesch, T. Weiss, M. Hentschel, and H. Giessen, "Infrared perfect absorber and its application as plasmonic sensor," *Nano Lett.* **10**(7), 2342–2348 (2010).
13. C. H. Liu, M. H. Hong, H. W. Cheung, F. Zhang, Z. Q. Huang, L. S. Tan, and T. S. A. Hor, "Bimetallic structure fabricated by laser interference lithography for tuning surface plasmon resonance," *Opt. Express* **16**(14), 10701–10709 (2008).

14. Q. Hao, B. K. Juluri, Y. B. Zheng, B. Wang, I. Chiang, L. Jensen, V. Crespi, P. C. Eklund, and T. J. Huang, "Effects of intrinsic fano interference on surface enhanced raman spectroscopy: comparison between platinum and gold," *J. Phys. Chem. C* **114**(42), 18059–18066 (2010).
15. Z. Liu, S. Durant, H. Lee, Y. Pikus, Y. Xiong, C. Sun, and X. Zhang, "Experimental studies of far-field superlens for sub-diffractive optical imaging," *Opt. Express* **15**(11), 6947–6954 (2007).
16. H. Hu, C. Ma, and Z. Liu, "Plasmonic dark field microscopy," *Appl. Phys. Lett.* **96**(11), 113107 (2010).
17. H. Tao, N. I. Landy, C. M. Bingham, X. Zhang, R. D. Averitt, and W. J. Padilla, "A metamaterial absorber for the terahertz regime: design, fabrication and characterization," *Opt. Express* **16**(10), 7181–7188 (2008).
18. B. K. Juluri, S. C. Lin, T. R. Walker, L. Jensen, and T. J. Huang, "Propagation of designer surface plasmons in structured conductor surfaces with parabolic gradient index," *Opt. Express* **17**(4), 2997–3006 (2009).
19. Y. Zhao, S. C. Lin, A. A. Nawaz, B. Kiraly, Q. Hao, Y. Liu, and T. J. Huang, "Beam bending via plasmonic lenses," *Opt. Express* **18**(22), 23458–23465 (2010).
20. M. Diem, T. Koschny, and C. M. Soukoulis, "Wide-angle perfect absorber/thermal emitter in the terahertz regime," *Phys. Rev. B* **79**(3), 033101 (2009).
21. Y. B. Zheng, T. J. Huang, A. Y. Desai, S. J. Wang, L. K. Tan, H. Gao, and A. C. H. Huan, "Thermal behavior of localized surface plasmon resonance of Au/TiO<sub>2</sub> core/shell nanoparticle arrays," *Appl. Phys. Lett.* **90**(18), 183117 (2007).
22. J. Henzie, J. Lee, M. H. Lee, W. Hasan, and T. W. Odom, "Nanofabrication of plasmonic structures," *Annu. Rev. Phys. Chem.* **60**(1), 147–165 (2009).
23. T. C. Chong, M. H. Hong, and L. P. Shi, "Laser precision engineering: from microfabrication to nanoprocessing," *Laser Photonics Rev.* **4**(1), 123–143 (2010).
24. X. Wang, C. Lao, E. Graugnard, C. J. Summers, and Z. L. Wang, "Large-size liftable inverted-nanobowl sheets as reusable masks for nanolithography," *Nano Lett.* **5**(9), 1784–1788 (2005).
25. Q. Hao, Y. Zeng, X. Wang, Y. Zhao, B. Wang, I. Chiang, D. H. Werner, V. Crespi, and T. J. Huang, "Characterization of complementary patterned metallic membranes produced simultaneously by a dual fabrication process," *Appl. Phys. Lett.* **97**(19), 193101 (2010).
26. V. G. Kravets, F. Schedin, and A. N. Grigorenko, "Plasmonic blackbody: almost complete absorption of light in nanostructured metallic coatings," *Phys. Rev. B* **78**(20), 205405 (2008).
27. V. G. Kravets, S. Neubeck, and A. N. Grigorenko, "Plasmonic blackbody: strong absorption of light by metal nanoparticles embedded in a dielectric matrix," *Phys. Rev. B* **81**(16), 165401 (2010).
28. Y. Tang, J. A. Bossard, D. H. Werner, and T. S. Mayer, "Single-layer metallodielectric nanostructures as dual-band midinfrared filters," *Appl. Phys. Lett.* **92**(26), 263106 (2008).
29. Z. H. Jiang, S. Yun, F. Toor, D. H. Werner, and T. S. Mayer, "Conformal dual-band near-perfectly absorbing mid-infrared metamaterial coating," *ACS Nano ASAP*, 10.1021/nn2004603 (2011).
30. K. A. Willets and R. P. Van Duyne, "Localized surface plasmon resonance spectroscopy and sensing," *Annu. Rev. Phys. Chem.* **58**(1), 267–297 (2007).
31. E. Hutter and J. H. Fendler, "Exploitation of localized surface plasmon resonance," *Adv. Mater. (Deerfield Beach Fla.)* **16**(19), 1685–1706 (2004).
32. M. J. Dodge, "Refractive properties of magnesium fluoride," *Appl. Opt.* **23**(12), 1980–1985 (1984).
33. P. Berini, "Plasmon polariton modes guided by a metal film of finite width," *Opt. Lett.* **24**(15), 1011–1013 (1999).
34. F. D. T. D. Lumerical, <http://www.lumerical.com/>, licensed to PSU BioNEMS Group.
35. W. Cai, U. K. Chettiar, H. K. Yuan, V. C. de Silva, A. V. Kildishev, V. P. Drachev, and V. M. Shalaev, "Metamagnetics with rainbow colors," *Opt. Express* **15**(6), 3333–3341 (2007).

## 1. Introduction

Light absorption in plasmonic nanostructures has recently attracted significant interest in the research community for applications such as solar cells [1–3], metamaterials [4–8], photodetectors [9,10], sensors [11–14], nanoimaging devices [15–19], and thermal emitters [20,21]. Various nanostructures with enhanced absorption have been proposed utilizing state-of-the-art nanofabrication techniques [22–25]. Kravets *et al* investigated high-efficiency absorption in a plasmonic blackbody using a composite grating nanostructure [26]. Nearly complete absorption was observed in the structure at a wide-range of wavelengths and incident angles; however, the optical properties of the one-dimensional refractory metallic coatings were strongly polarization-dependent. Following this work, Kravets *et al* introduced another design consisting of embedded silver nanoparticles in an Al<sub>2</sub>O<sub>3</sub> dielectric matrix [27]; the light scattered by the nanoparticles was trapped inside the dielectric matrix, demonstrating an effective absorption near unity. Na *et al* extended the design concept from a single-layer structure to a multi-layer structure and proposed a design in the infrared range for sensing applications [12]. They demonstrated, both experimentally and computationally, nearly zero reflection in a metal-dielectric-metal structure working in the infrared wavelength regime. Although the aforementioned designs exhibit excellent absorption efficiencies, they are constrained with issues such as relatively narrow working ranges, lack of reconfigurability, or

strong polarization dependence. One straightforward way to increase the working range of a plasmonic absorber is to introduce another absorption band into the spectrum by incorporating a functional layer into the structure [28,29]. The complex design and fabrication, however, have thus far restricted the wide application of this approach.

In this article, we design and fabricate a dual-band perfect plasmonic absorber with reconfigurable band positions. Our design exhibits multiple advantages over other plasmonic absorbers: a wide working range, incident angle insensitivity, simple reconfigurability, polarization independence, and easy fabrication process. We believe that such a design will enhance the functionality of plasmonic absorbers and be valuable in many applications such as sensors, solar cells, and metamaterials.

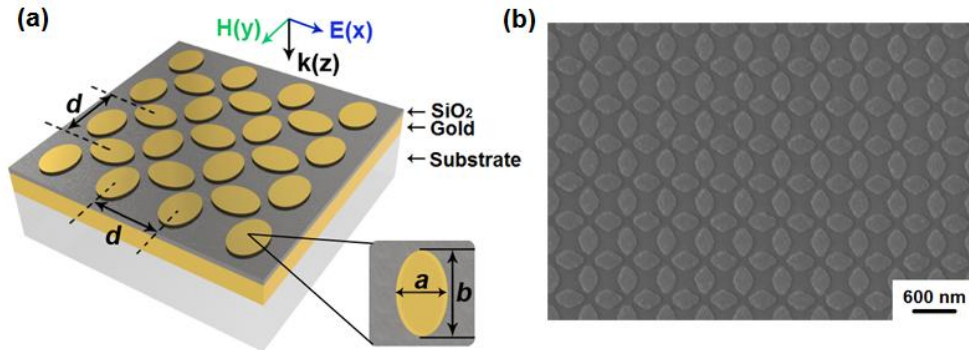


Fig. 1. (a) Schematic of the dual-band perfect absorber structure and the incident polarization configuration. (b) A SEM image of the designed structure.

## 2. Structure design

A schematic and SEM image of our dual-band absorber are shown in Fig. 1. The physical origin of near perfect absorption is the localization of electric and magnetic dipole resonances in the metal-dielectric-metal structure. The dual-band absorption was realized using elliptical nanodisks, which possess two resonance peaks associated with their major and minor axes [30,31]. We eliminated the polarization affinity by carefully arranging the elliptical nanodisks in a two-dimensionally symmetric structure. As shown in Fig. 1, our structure consists of three functional layers comprised of a dielectric layer sandwiched between two metal layers. The top metal layer is a 20 nm thick elliptical gold nanodisk array, where  $a$  denotes the length of each nanodisk's minor elliptical axis,  $b$  represents the length of the nanodisk's major axis, and  $d$  corresponds to the period along both  $x$  and  $y$  directions. The design parameters ( $a$ ,  $b$ , and  $d$ ) can be selectively tuned to demonstrate control of the structure's optical properties. The center spacing layer provides a large impedance mismatch between the constituent material and the metal claddings. Here, dielectric materials with relatively low permittivity, such as  $\text{SiO}_2$ ,  $\text{MgF}_2$ , or other polymer materials, are ideal candidates for high absorption [32,33]. For the real fabrication process, we choose  $\text{SiO}_2$  as the spacing layer to verify our design. Figure 1 (b) shows a SEM image of our structure. We can see the pattern of the nanodisks shows a good uniformity along both the  $x$  and  $y$  directions. The thickness of the dielectric layer is crucial because it affects the dipole resonance; as thickness increases, the resonance effect is diminished and the overall absorption efficiency is reduced. We optimize the performance of the perfect absorber with a 30 nm thick  $\text{SiO}_2$  layer and a 150 nm gold bottom functional layer. This thickness is larger than the penetration depth of electromagnetic waves in the infrared regime, and will block any incident light transmitted through the first two layers, leading to nearly zero transmission in the working range of the dual-band absorber. Another function of the thick gold mirror is to interact with the upper nanodisks to form electric and magnetic dipoles which couple the incident electromagnetic energy inside the structure. Therefore, near perfect absorption is obtained ( $A = 1 - R - T$ ).

### 3. Results and discussion

#### 3.1. Nearly perfect dual-band absorption

To numerically investigate the performance of our design, we employed a commercial software package (Lumerical) utilizing finite difference time domain (FDTD) methods [34]. In our simulation, the material property of gold was chosen from the software database (Gold (Johnson and Christy)) and the permittivity of  $\text{MgF}_2$  was set to 1.9. Periodic boundary conditions were used for both  $x$  and  $y$  directions, and a perfect matching layer boundary condition was used for the  $z$  direction. The mesh size was 8 nm in both  $x$  and  $y$  directions and 2 nm in  $z$  direction. We used a long simulation time of 1000 fs with a step of 0.006 fs to provide reliable results. We set the auto-cutoff value to  $1 \times 10^{-6}$  in our simulation which can be further decreased to get results even closer to the ideal case. Figure 2 (a) shows the reflection and transmission spectra under normally incident electromagnetic plane waves with the fixed polarization state given in Fig. 1 (a). In the simulation, the thickness of the top layer elliptical gold nanodisk array is 20 nm; the periods along both  $x$  and  $y$  directions are 600 nm; the minor and major axes of the elliptical gold nanodisks are  $a = 240$  nm and  $b = 360$  nm, respectively; and the bottom gold layer is 150 nm. The  $\text{SiO}_2$  dielectric spacer between the two metal layers is 30 nm thick. With these optimized design parameters, nearly zero transmission is obtained within the whole working range of the dual-band absorber, and two perfect absorption peaks are obtained at  $\lambda_1 = 1247$  nm ( $A_1 = 99.5\%$ ) and  $\lambda_2 = 1697$  nm ( $A_2 = 99\%$ ). To detail the overall incident wave absorption, the reflection and transmission spectra were also plotted in logarithmic (dB) scale in Fig. 2 (b)

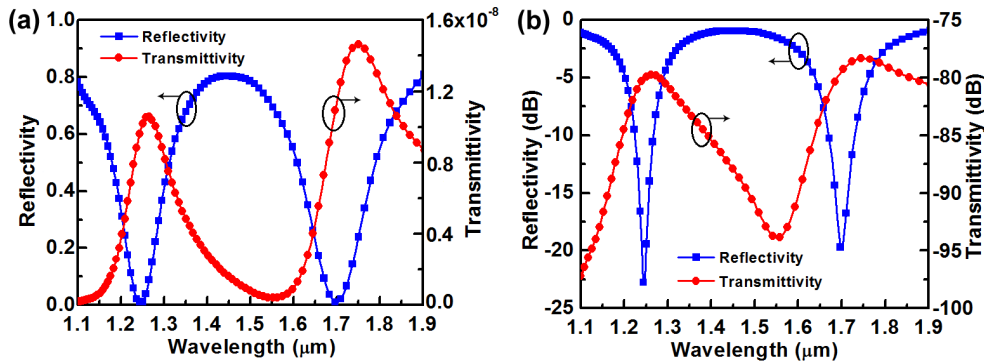


Fig. 2. The reflection and transmission spectra under normally incident electromagnetic plane waves with the fixed polarization state given in Fig. 1 (a). Results are shown in linear scale (a) and logarithmic (dB) scale (b), respectively.

We further investigate our dual-band absorber by changing the dimensions of the elliptical nanodisks which enables a repositioning of the absorption peaks while maintaining their dual-band characteristics. Figure 3 (a) shows a tunable range of resonant frequency which was modeled up to 700 nm without optimizing the period of the nanodisk array. For  $a = 240$  nm and  $b = 360$  nm, nearly zero reflectance was achieved at the wavelengths  $\lambda_1 = 1247$  nm and  $\lambda_2 = 1697$  nm. More than 99% absorbance is obtained at both of the resonance frequencies. Increasing the size of nanodisks causes a red shift of the absorption peaks, which is due to the red shift of the plasmonic resonance in each particle with increasing size, in addition to the red shift associated with a decrease in space between particles. For  $a = 270$  nm and  $b = 390$  nm, the two resonance wavelengths shift to  $\lambda_1 = 1372$  nm and  $\lambda_2 = 1824$  nm, respectively. For larger nanoparticle sizes,  $a = 300$  nm and  $b = 420$  nm, the two resonance wavelengths move further to  $\lambda_1 = 1484$  nm and  $\lambda_2 = 1954$  nm, respectively. We also investigated individual band control by changing the size of only one axis of the elliptical nanoparticle. The result in Fig. 3 (b) shows that the two absorption bands could also be adjusted individually which indicates the great flexibility of our dual-band absorber over the near infrared regime.

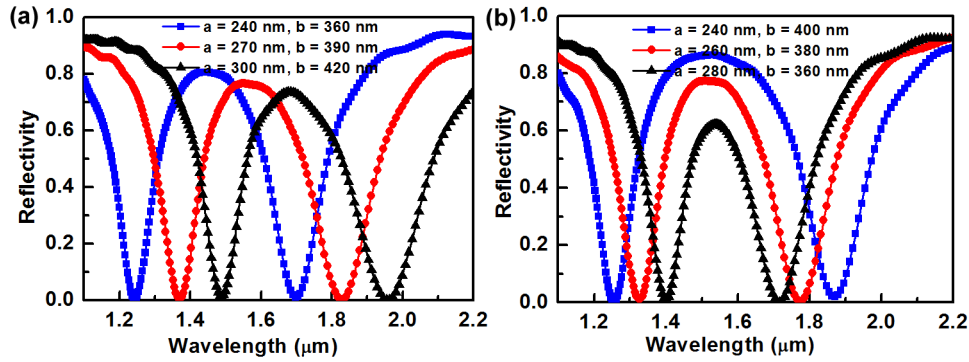


Fig. 3. Simulated reflectance spectra of the designed absorber structure at normal incidence with different dimensions of the elliptical gold nanoparticles. A 700 nm tunable range can be conveniently achieved by engineering the sizes of the gold nanoparticles on the top layer. The two absorption peaks can be easily tuned both (a) in parallel and (b) individually.

We conducted additional simulations to investigate the angle dependence of our dual-band plasmonic absorber. For oblique incidence, because there will be a phase shift for the incident electromagnetic field between each period, we used Bloch boundary conditions in the  $x$ -direction (propagation direction) for both TE and TM polarization, while maintaining all other aforementioned parameters. Figure 4 shows the absorptivity as a function of both wavelength and angle of incidence under TE and TM polarizations. The two red strips in the figure indicate the two angle-independent high absorption bands. Under both TE and TM polarizations, for incident angles ( $\theta$ ) up to 50 degrees, more than 95% absorption is still obtained for both of the two resonance peaks while maintaining the center frequencies. To detail the absorption peak value degradation between normal incidence and large angle incidence, the absorption efficiencies of different angles for each peak under TE and TM polarization are listed in Table 1.

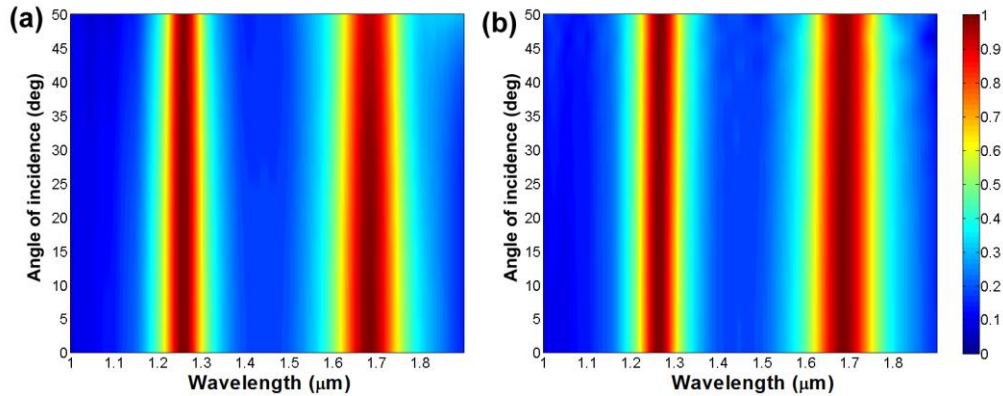


Fig. 4. The simulated absorption efficiencies as a function of wavelength and angle of incidence under (a) TE and (b) TM polarization.

**Table 1. Absorption efficiencies of different angles for each peak under TE and TM polarization**

	0	10	20	30	40	50
Peak 1 (TE)	99.5%	99.5%	99.4%	99.4%	99.2%	99.2%
Peak 1 (TM)	99.5%	99.5%	99.5%	99.4%	99.4%	99.4%
Peak 2 (TE)	99.0%	98.7%	98.5%	98.2%	96.6%	95.1%
Peak 2 (TM)	99.0%	98.8%	98.8%	98.7%	98.6%	98.5%

### 3.2. Nanofabrication and experimental measurement

The sample (Fig. 1 (b)) was fabricated using standard lift-off electron-beam lithography [25]. First, a 150 nm thick gold mirror is thermally evaporated on a clean glass substrate, then a 30 nm thick SiO<sub>2</sub> film is deposited on the top of the bottom gold layer. Electron-beam lithography and a metal lift-off process are used to define the elliptical gold nanodisks on the top layer. The major and the minor axes of the gold elliptical nanodisks are approximately 360 nm and 240 nm, respectively. Also, 2 nm chromium layers are deposited between each gold/SiO<sub>2</sub> interface to promote adhesion. The reflectivity of the fabricated dual-band absorber at normal incidence is measured with a Fourier transform IR (FTIR) spectrometer (Bruker IFS 66/S) equipped with a liquid nitrogen cooled, mercury cadmium telluride detector.

The measured and simulated results under TE and TM polarization are shown in Figs. 5 (a) and (b), respectively. The experimental measurements match well with the simulations and the absorber shows excellent insensitivity to incident polarization. The absorption peaks maintain their position for both longer and shorter resonance wavelengths under different polarizations. For the longer wavelength absorption peak, under both polarizations, the measured results show a resonance wavelength at  $\lambda_1 = 1703$  nm, matching well with simulations predicting 1679 nm, and the absorption efficiency is slightly reduced from the simulated 99% to 93.2%. For the shorter absorption peak, a 27 nm difference is observed between the simulations and experiments under both polarizations. The resonance wavelength moves from the simulated 1247 nm to the measured  $\lambda_2 = 1274$  nm and the absorption efficiency decreases to 89.3%. We believe that the slight shift of the absorption peaks comes from the fabrication deviations of the sizes of the elliptical nanoparticles. As we discussed in Fig. 3, a larger gold nanoparticle size will cause a red shift of the absorption peak; thus it is likely that the size of the fabricated sample is a little bit larger than the simulated parameter. The reduction in absorption efficiency can be mainly attributed to the 2 nm thick chromium layer between the gold/SiO<sub>2</sub> interfaces. These layers affect the magnetic resonance between the top gold nanoparticles and the bottom gold layers. Consequently, reduced absorption efficiency is obtained. Also, the roughness of the fabricated nanoparticle may be another reason to the loss of absorption. The surface roughness will not only increase the scattering, but also affect the thickness of the top layer nanodisk array which is essential to the magnetic dipolar resonance between the nanoparticle and bottom gold film. In addition, the periodic boundary conditions approximate an infinite array in the simulation while the experiment was measured with limited periods; this discrepancy will also affect the results. We may improve the performance of our device by choosing other dielectric layers for real fabrication, such as polymer materials, which have relative low permittivity and do not need adhesive layers.

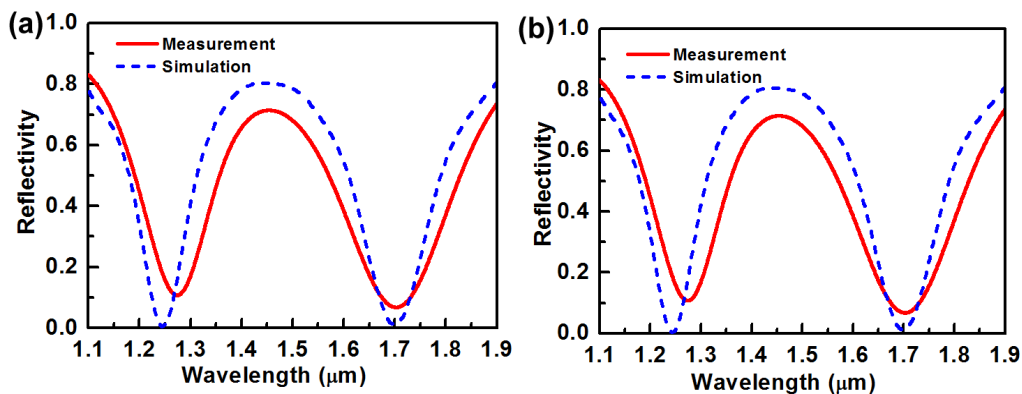


Fig. 5. Measured and simulated reflection spectra of the dual-band absorber under (a) TE polarization and (b) TM polarization at normal incidence.

Although the measured absorption efficiency does not perfectly match simulations, high absorption is still obtained for both of the two resonance frequencies; validating the design experimentally.

### 3.3. Mechanism of enhanced absorption

As stated above, the physical origin of the near perfect absorption in our structure is related to the electric dipolar resonance in the nanodisk array due to localized surface plasmon resonance and the magnetic dipolar resonance between the nanodisk array and gold film. To understand the nature of the magnetic and electric resonances, the charge distribution in multiple cross-sections of a single nanoparticle and the underlying structure were calculated at resonance wavelengths  $\lambda_1 = 1697$  nm (cross section given along major axis) and  $\lambda_2 = 1247$  nm (cross section given along minor axis). The results are given in Fig. 6(a) ( $\lambda_1$ ) and Fig. 6(b) ( $\lambda_2$ ). The charge distribution indicated that anti-parallel currents are formed in the elliptical gold

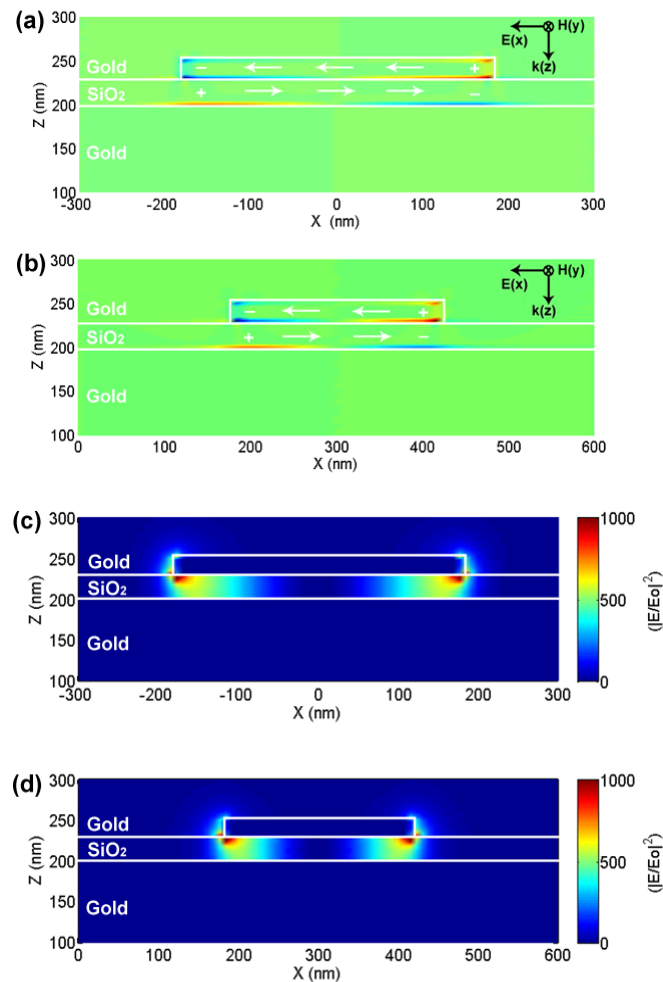


Fig. 6. Calculated charge and field distribution at resonances (a) (c)  $\lambda_1 = 1697$  nm (cross section given along major axis) and (b) (d)  $\lambda_2 = 1247$  nm (cross section given along minor axis) where perfect absorbance occur. Anti-parallel currents are indicated by the charge distribution and the enhanced electric fields are confined between the top gold nanodisks and the bottom gold mirror.

nanodisk and the bottom gold layer creating circulating currents between the two metal layers. This circulating current is known as a magnetic resonance, which results in an artificial magnetic moment that interacts strongly with the magnetic field of the incident light [35]. Therefore, strong enhancements of the localized electromagnetic fields are excited between the two metal layers at resonance frequencies. As a result, the incident electromagnetic energy can be efficiently confined to the intermediate dielectric spacer. In order to better understand the confined electromagnetic energy, the electric field distributions in the cross-sections along both major and minor axis of a single nanoparticle at the resonance wavelengths are showed in Fig. 6(c) and Fig. 6(d). In our absorber structure, the strongest electromagnetic interactions are obtained at these resonance wavelengths. The enhanced electric fields are confined between the top gold nanodisks and the bottom gold mirror and then transformed into heat. This effect leads to the nearly zero reflectance observed experimentally and computationally. Furthermore, we can confirm, from Fig. 5, that the two absorption wavelengths of our dual-band absorber originate from the interaction between the incident electromagnetic field and the elliptical gold nanoparticles along both the major and minor axes.

#### **4. Conclusion**

In conclusion, we experimentally and numerically demonstrate a dual-band perfect plasmonic absorber in the near-infrared frequency regime by utilizing a metal-dielectric-metal, three-layer nanostructure. Nearly 100% absorption peaks are obtained at the resonance frequencies with the device demonstrating nearly perfect polarization-independence at normal incidence, and maintaining near-perfect absorption at incident angles up to 50°. Moreover, a tunable range of the resonant frequency was modeled up to 700 nm by tuning the dimensions of the nanostructures. Experimental measurements show a good match with the simulation results. With its excellent performance, our design can be valuable in many applications such as solar cells, metamaterials, and sensing. Also, we believe that perfect absorbers in the visible regime, multi-band or broad-band with simple designs are interesting directions to pursue in future work.

#### **Acknowledgments**

We gratefully acknowledge the financial support from the Air Force Office of Scientific Research (AFOSR), National Science Foundation (NSF), Beijing Institute of Technology (BIT), China Scholarship Council (CSC), and the Penn State Center for Nanoscale Science (MRSEC). Components of this work were conducted at the Penn State node of the NSF-funded National Nanotechnology Infrastructure Network (NNIN).